

Article

Thermal Conductivity and Wear Behavior of HVOF-Sprayed Fe-Based Amorphous Coatings

Haihua Yao ¹, Zheng Zhou ^{1,*}, Liang Wang ¹, Zhen Tan ¹, Dingyong He ¹ and Lidong Zhao ²

¹ College of Materials Science and Engineering, Beijing University of Technology, Beijing 100124, China; yaohh06@163.com (H.Y.); s201409001@emails.bjut.edu.cn (L.W.); zhen.tan@bjut.edu.cn (Z.T.); dyhe@bjut.edu.cn (D.H.)

² Surface Engineering Institute, RWTH Aachen University, 52062 Aachen, Germany; zhao@iot.rwth-aachen.de

* Correspondence: zhouzhengbjut@bjut.edu.cn; Tel.: +86-10-6739-2168

Academic Editor: Alessandro Lavacchi

Received: 16 August 2017; Accepted: 17 October 2017; Published: 19 October 2017

Abstract: To protect aluminum parts in vehicle engines, metal-based thermal barrier coatings in the form of Fe₅₉Cr₁₂Nb₅B₂₀Si₄ amorphous coatings were prepared by high velocity oxygen fuel (HVOF) spraying under two different conditions. The microstructure, thermal transport behavior, and wear behavior of the coatings were characterized simultaneously. As a result, this alloy shows high process robustness during spraying. Both Fe-based coatings present dense, layered structure with porosities below 0.9%. Due to higher amorphous phase content, the coating H-1 exhibits a relatively low thermal conductivity, reaching 2.66 W/(m·K), two times lower than the reference stainless steel coating (5.85 W/(m·K)), indicating a good thermal barrier property. Meanwhile, the thermal diffusivity of amorphous coatings display a limited increase with temperature up to 500 °C, which guarantees a steady and wide usage on aluminum alloy. Furthermore, the amorphous coating shows better wear resistance compared to high carbon martensitic GCr15 steel at different temperatures. The increased temperature accelerating the tribological reaction, leads to the friction coefficient and wear rate of coating increasing at 200 °C and decreasing at 400 °C.

Keywords: amorphous coating; microstructure; thermal conductivity; wear behavior

1. Introduction

During the last few decades, aluminum alloy replacing steel components has developed gradually for weight reduction of vehicle engines. However, the relatively low melting point and poor wear resistance of aluminum alloys were compelled to face in application. Thermally-sprayed coatings are considered an effective way to alleviate these issues simultaneously [1–4], especially for thermal barrier coatings (TBCs). It is well-known that many ceramic as TBCs materials, for instance yttria-stabilized zirconia (YSZ), and display excellent thermal insulating properties and high hardness. Nevertheless, the inherent brittle characteristic of these materials may reduce the reliability of their coatings, or even cause catastrophic failure under mechanical loading or thermal shock [4–6]. Moreover, the coefficients of thermal expansion (CTE) of ceramic are much lower than that of aluminum alloys, which may lead to a mismatching problem during elevated temperatures [2]. Therefore, there is a rising interest in developing metal-based thermal barrier coatings (MBTBCs) to overcome the defects of ceramic-based thermal barrier coatings (CBTBCs). Generally, metals are known as good thermal and electrical conductors due to the existence of free electrons. To restrict the free electron contribution to thermal conductivity of MBTBCs, amorphous metallic coatings exhibit potential applications because of their high densities of scattering defects. Consequently, Fe-based amorphous coatings seem to be the most promising candidate, mainly consulting the glass-forming ability, wear resistance, and cost efficiency.

With regard to Fe-based amorphous coatings extensive research has been focused on their wear and corrosive behaviour [7–13]. Little attention has been paid to the thermal transport behaviour of Fe-based amorphous coatings because of their metastable state. In recent years, a few valuable attempts have been conducted on Fe-based amorphous coatings for MBTBCs application. As expected, the amorphous coatings can display a relatively low thermal conductivity and diffusivity. For example, Shin et al. [4,14] reported that the induction plasma-sprayed (IPS) Fe-based amorphous coating with a commercial powder showed low thermal conductivity of about 1.99 W/(m·K). It is an extremely low value in traditional metal-based coatings and close to conventional ceramic coating (YSZ). Poirier et al. [2] assessed the potential of atmosphere plasma spraying (APS) amorphous-type coatings and conventional arc-sprayed steel coatings as TBCs. They found that the APS Fe-based amorphous coating exhibits a lower thermal conductivity of 2.4–2.7 W/(m·K) but poorer spalling resistance than those of conventional arc-sprayed steel coatings under thermal cycling. Bobzin et al. [15,16] prepared a series of Fe-based amorphous/nanocrystalline coatings using HVOF and APS, respectively. They concluded the Fe-based amorphous coatings showed relatively low thermal diffusivity values in the range of 0.01–0.04 cm²/s and good thermal shock behavior.

Although the current Fe-based amorphous coatings could be potential candidates of MBTBCs due to their relatively low thermal conductive ability, further exploration of associated frictional performance should be considered. Coating resistance to wear is critical for vehicle engine applications where severe wear is present, such as piston rings and cylinder liners [3,17]. A good characterization and understanding of wear mechanisms with increased temperature are substantially meaningful to design the practical application of amorphous coatings. In this article, a cost-effective Fe₅₉Cr₁₂Nb₅B₂₀Si₄ alloy was chosen and manufactured to prepare amorphous coatings by the HVOF spraying process. The microstructure characteristic of the coatings obtained under different spraying parameters were investigated. The thermal conductivity and associated wear behavior at varied temperatures were detected and the potential of amorphous coatings as MBTBCs was evaluated.

2. Materials and Methods

A Fe₅₉Cr₁₂Nb₅B₂₀Si₄ powder was prepared by high-pressure gas atomization method from industrial grade materials including pure Cr (≥99.1 wt %), Fe (≥99.1 wt %), as well as pre-alloy Fe–Nb (Nb: 65 wt %), Fe–B (B: 19 wt %) and Fe–Si (Si: 75 wt %). The as-atomized powders were sieved to a fraction of 20–45 μm for spraying on commercial AISI 4032 aluminum substrate. Before spraying, all substrates were degreased by acetone, dried, and then grit-blasted. The Fe₅₉Cr₁₂Nb₅B₂₀Si₄ coatings were deposited by a JP5000 HVOF spraying system from Praxair (Danbury, CT, USA) under two different conditions with varied oxygen and fuel flow, but their ratio in all conditions was kept basically constant. The detailed spraying parameters are listed in Table 1.

Table 1. Spraying parameters employed in the HVOF process.

Specimen	Kerosene Flow (GPH)	Oxygen Flow (SCFH)	Nitrogen Flow (SCFH)	Feed Rate (r/min)	Spraying Distance (mm)
H-1	6.2	2000	26	5.0	380
H-2	6.8	2200	26	5.0	380

Two kinds of specimens were produced. The first coatings were deposited with target thickness of 400–500 μm, which were used to investigate the coating microstructure, bonding strength, and wear behavior. Nearly 1 mm thick coatings were also deposited on the aluminum plates and separated from the substrate to obtain free-standing coatings. These free-standing coatings with a diameter of 12.7 mm were used to measure the density and thermal diffusivity respectively, while with a mass of 20–30 mg for the measurements of heat capacity.

The structures of the powder and as-deposited coatings were analyzed by X-ray diffraction (XRD, D8 ADVANCE, Bruker, Billerica, MA, USA) with Cu K α radiation. The microstructures of

coatings were characterized by using scanning electron microscopy (SEM, Quanta FEG 650, FEI, Hillsboro, OR, USA) equipped with energy-dispersive X-ray analysis (EDX), and transmission electron microscopy (TEM, JEM 2100, JEOL, Tokyo, Japan). Fifteen cross-sectional micrographs of each coating were taken with an optical microscope (OM, BX51M, OLYMPUS, Tokyo, Japan) to evaluate the average porosity fraction using the Image J software (Image J-2). The oxygen content in detached coatings was analyzed by an oxygen/nitrogen determinator (G8 GALILEO, Bruker, Billerica, MA, USA). The thermal stability of the samples was examined by differential scanning calorimeter (DSC, STA 449F3, NETZSCH, Bobingen, Germany) in a continuous heating mode at a rate of 20 °C/min from room temperature to 1000 °C under an argon atmosphere.

The apparent density (ρ) of the sprayed coatings was measured by the Archimedes principle. Thermal diffusivity (α) measurement of the coatings was carried out by using the laser flash thermal constant analyzer (LFA427, NETZSCH, Bobingen, Germany). Specific heat (C_p) of the coatings was also measured using the differential scanning calorimetry (STA 449F3, NETZSCH, Bobingen, Germany). Then, the thermal conductivity (κ) was calculated from the relation $\kappa = \alpha\rho C_p$. In order to evaluate the thermal transport properties of amorphous coatings, commercially-available 316L stainless steel coating (Cr 18.02; Ni 11.91, Mo 2.27, Si 0.95, (S, P, N) < 0.17, Fe: balance, wt %) was used as reference coating, named H-316 coatings. The thermal transport measurements of H-316 coating were performed in the same way.

Vickers microhardness measurements were conducted on the cross section of the HVOF coating with an applied load of 100 gf and indentation time of 10 s, and calculated as an average of 15 measurements. The bonding strength of coating was detected using a universal mechanical test machine (QBD-100, Chembound Industrial Co., Ltd., Shaoguan, China) according to ASTM C633-01 standard [18]. The average value of the bonding strength of coating was calculated after three tests.

The friction and wear test was carried out using a standard SRV (Optimol Instruments Prüftechnik GmbH, Munich, Germany) wear tester under dry condition with reciprocating motion. A high carbon martensitic GCr15 steel ball (832 HV) [19] with a diameter of 10 mm was used as the friction counterpart. Prior to sliding tests, the as-deposited coating was ground and then finely polished with diamond paste. The sliding tests were conducted at a load of 30 N, stroke length of 1 mm, frequency of 20 Hz, duration of 30 min, and a temperature range of room temperature (RT) to 400 °C in the air. A new frictional pair was used for the sliding test under each pre-set temperature. The friction coefficient curves were recorded automatically using a computer connected with the friction and wear tester. The wear volume loss of both coatings and counterparts was measured using confocal scanning laser microscope (CSLM, Olympus 4100, Olympus, Tokyo, Japan). The wear rate is calculated as: $K = V/SF$ [20], where K is the wear rate with the unit of $\text{mm}^3/(\text{N}\cdot\text{m})$, V is the wear volume loss in mm^3 , S is the total sliding distance in m, and F is the normal load in N.

3. Results and Discussion

3.1. Microstructure

Figure 1 shows the SEM micrographs of the $\text{Fe}_{59}\text{Cr}_{12}\text{Nb}_5\text{B}_{20}\text{Si}_4$ feedstock powder. Apparently, the majority of Fe-based particles exhibit spherical or near-spherical shapes, providing good flow ability during the spraying process. The XRD patterns of the powder and as-deposited coatings under different spraying parameters are illustrated in Figure 2. It is notable that a broad halo peak appears in both the feedstock and coating, indicating the high amorphous phase content, which is mainly owing to the relatively high glass forming ability (GFA) of the $\text{Fe}_{59}\text{Cr}_{12}\text{Nb}_5\text{B}_{20}\text{Si}_4$ alloy system. This alloy meets well the three empirical rules proposed by Inoue et al. [21]. Namely, the present alloy is composed of more than three elements, the atomic size of the constituent elements decreases in the order of Nb (0.143 nm) > Fe (0.135 nm) > Cr (0.125 nm) > Si (0.117 nm) > B (0.07 nm), and the heats of mixing are negative for the main atomic pairs of Fe–Cr, Fe–Nb, Fe–Si, Fe–B, Nb–Si, and B–Nb corresponding to -1 , -16 , -35 , -26 , -56 , and -54 kJ/mol, respectively [22]. Consequently, highly-dense, randomly-packed atomic

configurations, higher viscosity, and lower atomic diffusivity are realized, leading to a high GFA [22,23]. Nevertheless, very weak crystalline peaks associated with borides are identified in the patterns of the Fe-based coatings.

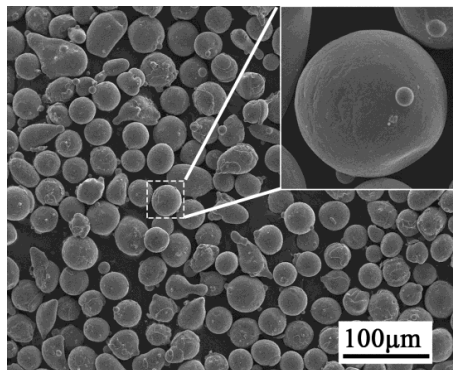


Figure 1. A typical SEM image of spraying powders of $\text{Fe}_{59}\text{Cr}_{12}\text{Nb}_5\text{B}_{20}\text{Si}_4$ alloy with 20–45 μm diameter.

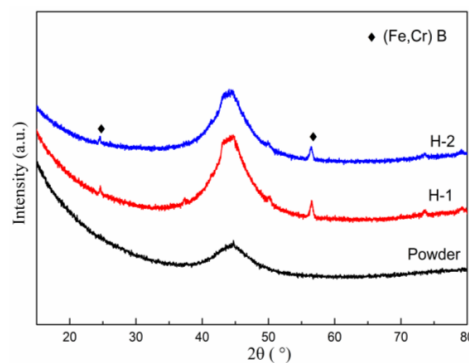


Figure 2. XRD patterns of the atomized powders and the as-deposited coatings.

Figure 3 reveals typical SEM micrographs from cross-sections of amorphous coatings and substrates. Therein, Figure 3a,b show low-magnification SEM micrographs of coating H-1 and H-2, respectively. Apparently, both of coatings exhibit a dense layered structure with good adherence to the substrate typical of HVOF thermally-sprayed deposits. Some fine pores are visible as dark regions marked in Figure 3a,b. The porosities of coatings were analyzed on optimal microscopy and listed in Table 2. The coating H-2 exhibits a slightly lower porosity of 0.6% compared to that of the coating H-1 with a value of 0.9%. This is mainly attributed to the higher particle velocity under the spray condition H-2. Nonetheless, both coatings remain of relatively low porosity, which is in accordance with the average level of conventional HVOF-sprayed amorphous coatings [23,24]. Under high-magnification SEM, some unmelted particles with limited deformation have been occasionally detected in the typical regions of coatings, as shown in Figure 3c. After etching with aqua regia, it is clear that crystallization occurred in the interior of unmelted particles while the exterior is an amorphous zone, as illustrated in Figure 3d. The reason for the formation of crystallites is mainly because some particles were partly melted. Figure 4 demonstrates a sketch of the partly-melted particles, namely, inside those particles was a solid state, while outside was a liquid state, with the existence of deformation. The unmolten fractions in particles experienced temperatures which are significantly higher than the crystallization (glass transition) temperature of this alloy. Hence, these partly-melted particles in Fe-based amorphous coatings could be responsible for the appearance of crystalline peaks in XRD patterns (Figure 2). Moreover, it is note that no obvious oxide inclusions are observed in both coatings micrographs. The analysis of the oxygen contents reveals that the feedstock material was slightly oxidized during spraying process (Table 2). The oxygen contents of coatings are in average of 0.16–0.18%, which are

very low for metallic coatings. The results reveal high process robustness during spraying of this amorphous alloy. The recognizable variation of the spray condition does not lead to a significant change in the coating microstructure.

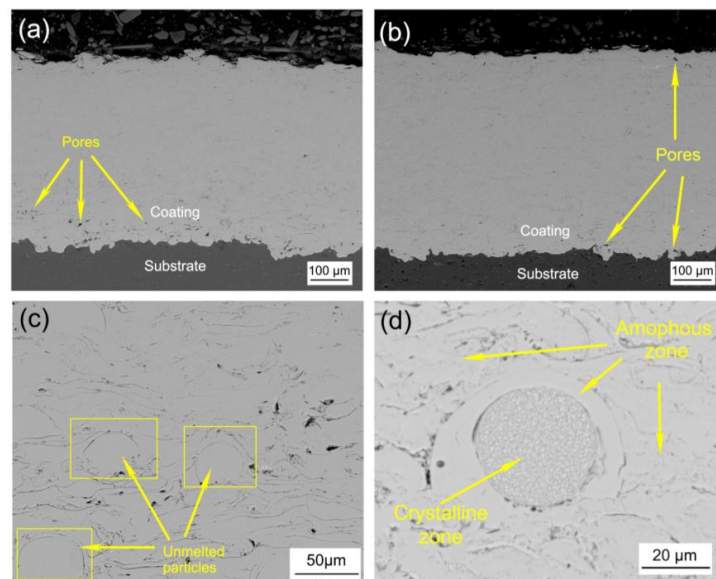


Figure 3. SEM micrographs of the cross-section of the as-deposited coatings: (a) low-magnification micrograph of coating H-1; (b) low-magnification micrograph of coating H-2; (c) high-magnification micrograph of typical region; (d) high-magnification micrograph of typically unmelted particle.

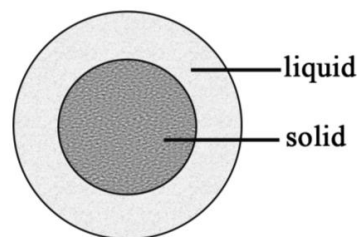


Figure 4. The sketch of partly melted particle.

Table 2. The porosity, oxygen content, and the crystallization temperature T_x measured by DSC of powders and coatings.

Specimen	Porosity (%)	Oxygen Content (wt %)	T_x (°C)	Amorphouscontent (%)
Powder	–	0.017 ± 0.005	643.7	100
H-1	0.9 ± 0.06	0.16 ± 0.001	633.6	62.4
H-2	0.6 ± 0.2	0.18 ± 0.002	632.2	55.2

To obtain more detailed information on the microstructure of $\text{Fe}_{59}\text{Cr}_{12}\text{Nb}_5\text{B}_{20}\text{Si}_4$ coating, the H-1 coating was investigated using TEM. The bright-field image and diffused halo ring in SAED pattern sited in Figure 5a verifies that the H-1 coating is basically composed of amorphous phase. Meanwhile some nanocrystals with grain sizes smaller than 50 nm can also be identified, as shown in Figure 5b. These precipitated nanocrystals distribute in the amorphous matrix, which could be caused by the decreased cooling rate of spraying compared to powder manufacturing process. In addition, the heat accumulated inside the coatings during spraying might lead to the generation of the nanocrystals [23]. Therefore, the crystalline peaks identified in XRD patterns (Figure 2) could be associated with the partly melted particles (Figure 3c,d) and the generation of nanocrystals (Figure 5b).

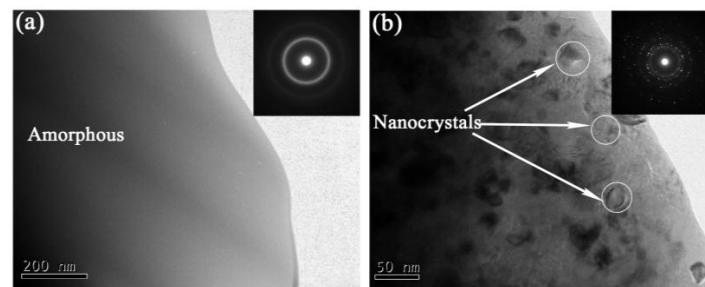


Figure 5. Bright-field TEM image and selected area electron diffraction (SAED) patterns of the as-deposited H-1 coating: (a) amorphous state and (b) nanocrystalline state.

To further clarify the amorphous contents of coatings quantitatively, DSC measurement for powders and the as-deposited coatings were carried out and illustrated in Figure 6. The content of amorphous phase (Am. %) in the coatings is calculated according to the followed equation [23]:

$$\text{Am. \%} = \Delta H_{\text{coating}} / \Delta H_{\text{powder}} \quad (1)$$

where $\Delta H_{\text{coating}}$ and ΔH_{powder} represent the heat of crystallization for coating and powder, respectively. It is assumed that the powder has a fully-amorphous structure thereat. The results are also presented in Table 2, as well as the crystallization temperature T_x . As can be seen, the H-1 coating exhibits a higher amorphous content compared to the H-2 coating. This is attributed to the larger thermal effect of the gas jet during the spraying process, and a similar variation for $\text{Fe}_{48}\text{Cr}_{15}\text{Mo}_{14}\text{C}_{15}\text{B}_6\text{Y}_2$ coatings had been reported in our previous study [23]. However, with respect to the large difference in the spray parameter, the limited variation in the amorphous content confirms this amorphous alloy exhibiting high process robustness. In addition, the crystallization temperature (T_x) of the coatings are higher than $630\text{ }^\circ\text{C}$, manifesting that these amorphous coatings have high thermal stability against crystallization, which could guarantee a reliable and wide usage on aluminum alloys.

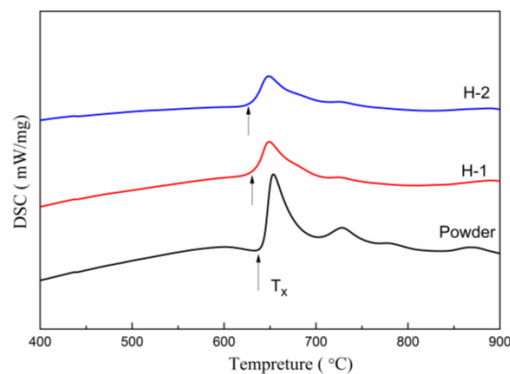


Figure 6. DSC traces of the powder and as-deposited coatings H-1 and H-2.

3.2. Thermal Transport Behavior

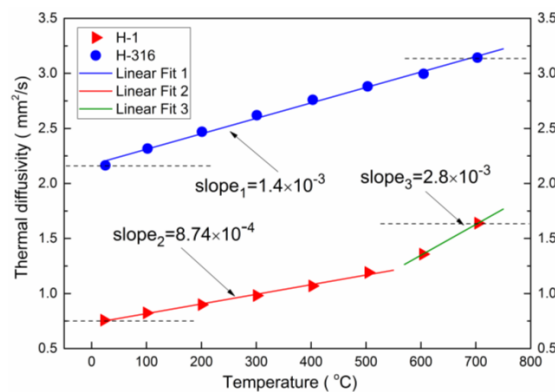
It is regarded that stainless steel displays one of the lowest thermal conductivity among conventional alloys, about $15\text{ W}/(\text{m}\cdot\text{K})$ [19]. Thereby, commercial 316L stainless steel coating (denoted as H-316) was chose and deposited by HVOF under the same spraying parameter of H-1 to evaluate the thermal conductive properties of Fe-based amorphous coating. The phase structure of the H-316 coating is composed of γ -(Fe,Ni) and iron oxide phase composition, which is in agreement with the previous report [25,26]. The calculated thermal conductivities (κ) of the coatings are given in Table 3.

Table 3. The densities, thermal capacities, thermal diffusivities, and thermal conductivities of coatings.

Specimen	ρ (g/cm ³)	C_p (J/g·K) $\times 10^{-1}$	α (mm ² /s)	κ (W/(m·K))
H-1	6.88	5.03	0.77	2.66
H-2	7.03	5.15	0.85	3.05
H-316	7.29	4.75	1.69	5.85

Clearly, the thermal conductivities of the amorphous coatings are much less than that of the reference H-316 coating ($\kappa = 5.85$ W/(m·K)). The coating H-1 exhibits the lowest thermal conductivity among the coatings, two times lower than that of the H-316 coating, indicating a good thermal barrier performance. According to the elementary kinetic theory $\kappa = 1/3cvl$ [27], the thermal conductivity (κ) is highly related to the mean free path (l) of phonons. However, the mean free path in disorder structure is usually limited to the dimensions of the atomic units [4]. Moreover, the existence of numerous vacancy defects in disorder [28–30], makes the scattering of phonon and electron become more intensive. These factors lead to the lower thermal conductivities of amorphous Fe₅₉Cr₁₂Nb₅B₂₀Si₄ coatings. The higher amorphous phase content of the coating H-1 gives rise to its lower thermal conductivity compared the coating H-2. Since the porosities and oxygen contents of both coatings are very low, the effects of porosity and oxide on the thermal conductivity are correspondingly lower.

Figure 7 shows the change in the thermal diffusivity (α) of H-1 and H-316 coating with temperature, together with the fitting curve as solid line. Obviously, the thermal diffusivities of both HVOF-sprayed coatings increase with temperature, showing typically positive temperature coefficient of metallic materials. The linear fitting slope represents the growth rate of α via temperature. Apparently, α of the H-316 coating shows a continuous increase from 2.16 to 3.14 mm²/s and the slope is 1.4×10^{-3} mm²/s·°C. The thermal diffusivity, α value of H-1 coating increases in multistage. At the temperature below 500 °C, α value increases with a very low slope of 8.74×10^{-4} mm²/s·°C. At 600 °C, α value rises abruptly from 1.19 mm²/s at 500 °C to 1.36 mm²/s, and up to 1.64 mm²/s at 700 °C, with a larger slope of 2.8×10^{-3} mm²/s·°C. This could be attributed to the change of amorphous phase. As temperature elevates into supercooled liquid region even above T_x ($T_g = 595$ °C, $T_x = 633$ °C), more atoms begin to rearrange for devitrification and a subsequent phase transformation from amorphous to crystalline took place. This microstructural change brought about a reduction of scattering intensity of electrons and phonons, making an increase of their mean free path, further leading to a larger ascent of thermal diffusivity at 700 °C. This multistage growth behavior in thermal transport of amorphous coating versus temperature is similar to Zr-based and Fe-based BMG previously reported [29,31,32]. Nevertheless, the Fe-based amorphous coating maintains much lower value of α than the stainless steel coating in the whole examined temperature range.

**Figure 7.** The change of thermal diffusivity of HVOF-sprayed coatings versus temperature, together with linear fit curves.

3.3. Wear Behavior

To evaluate the wear behavior of the $\text{Fe}_{59}\text{Cr}_{12}\text{Nb}_5\text{B}_{20}\text{Si}_4$ amorphous coating with increased temperature, the wear test was done with the H-1 coating at room temperature (RT), 200 °C and a relatively high temperature of 400 °C, respectively. The microhardness and bonding strength of the H-1 coating are determined prior to the wear test. The microhardness of the H-1 coating amounts to $1072 \pm 90 \text{ HV}_{0.1}$, as well as the bonding strength is $48.6 \pm 1.4 \text{ MPa}$.

Figure 8 shows the friction coefficient as a function of sliding duration for the H-1 amorphous coating at different temperatures. It is found that the steady state value of friction coefficient is the highest at 200 °C and the lowest at 400 °C. The determined wear rate of coating amounts to $1.97 \times 10^{-5} \text{ mm}^3/(\text{N}\cdot\text{m})$ for room temperature, $3.82 \times 10^{-5} \text{ mm}^3/(\text{N}\cdot\text{m})$ for 200 °C, and $1.12 \times 10^{-5} \text{ mm}^3/(\text{N}\cdot\text{m})$ for 400 °C, as illustrated in Figure 9.

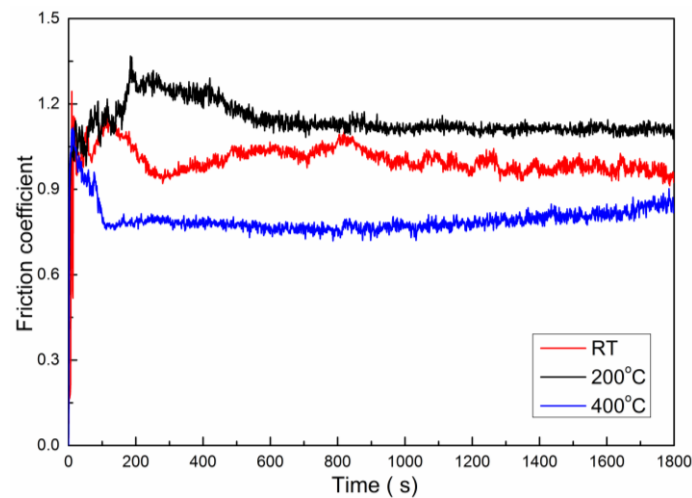


Figure 8. The friction coefficients of the $\text{Fe}_{59}\text{Cr}_{12}\text{Nb}_5\text{B}_{20}\text{Si}_4$ amorphous coating at different temperatures.

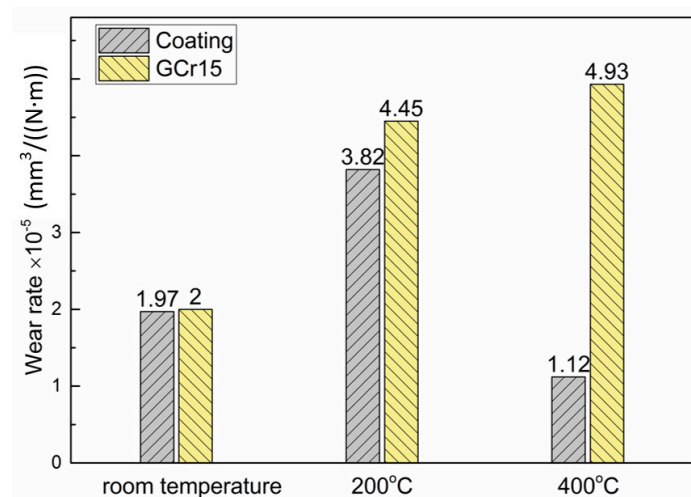


Figure 9. The wear rate of amorphous coatings and GCr15 steel ball at different temperatures.

The wear rates of amorphous coating are in good agreement with the friction coefficients, namely the wear at 200 °C caused the highest wear loss and friction coefficient, while at 400 °C both values are the lowest. However, the wear rates of friction counterparts (GCr15 steel ball) increase with temperature, corresponding to $2.0 \times 10^{-5} \text{ mm}^3/(\text{N}\cdot\text{m})$ for room temperature, $4.45 \times 10^{-5} \text{ mm}^3/(\text{N}\cdot\text{m})$ for 200 °C, and $4.93 \times 10^{-5} \text{ mm}^3/(\text{N}\cdot\text{m})$ for 400 °C, as shown in Figure 9. It is notable that the wear

rate of counterparts is higher than that of coatings at each temperature. This indicates that the Fe-based amorphous coating exhibits a better wear resistance compared to the high carbon martensitic GCr15 steel.

In order to reveal the wear mechanism, the worn surface morphologies of coatings were examined by SEM coupled with EDX, and shown in Figures 10–12. As shown in Figure 10, the worn surface of the H-1 coating after sliding at room temperature is relatively smooth (Figure 10a). Since both the H-1 coating and the GCr15 steel ball are hard, abrasion wear played an important role. The grooves caused by abrasion are low (Figure 10b), due to the relatively small difference in the hardness of the counterparts. As identified by EDX analysis, the counterparts and wear debris were oxidized by the friction induced heat. However, the oxidized debris was not compacted on the wear track, because they were still brittle at the test conditions. As a result, the coating surface is slightly covered by oxide debris (Figure 10a). The EDX measurements at points 1 and 2 (Figure 10c,d) confirm the uncovered surface and oxidized debris. In addition, flaked lamellae are recognizable, indicating that the fatigue also contributed to the wear.

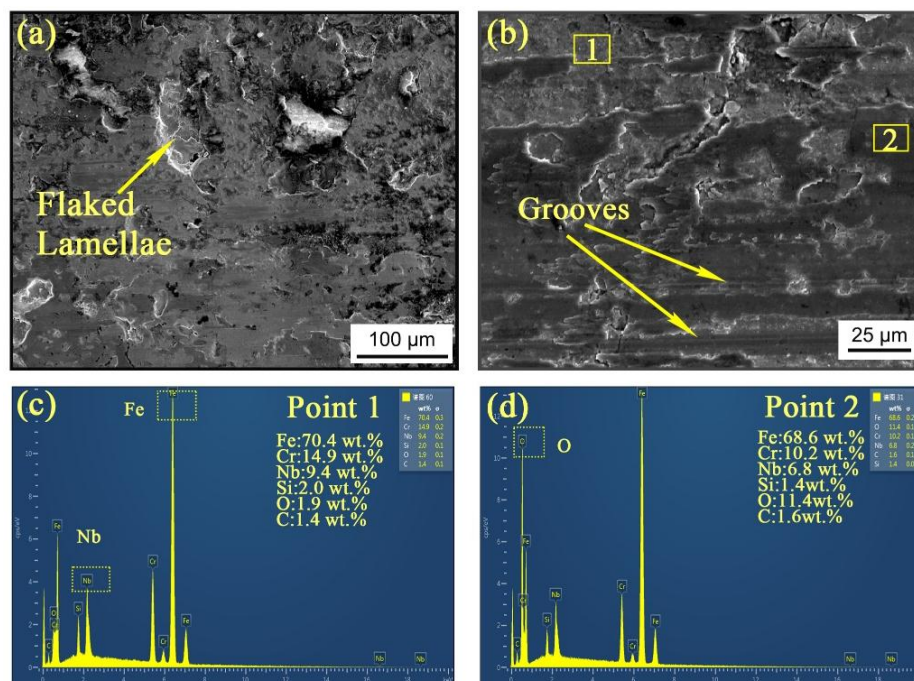


Figure 10. Typical worn surface morphologies and EDX results of $\text{Fe}_{59}\text{Cr}_{12}\text{Nb}_5\text{B}_{20}\text{Si}_4$ amorphous coating after sliding at room temperatures: (a) low-magnification; (b) high-magnification; (c) EDX result of point 1; and (d) EDX result of point 2.

Figure 11 shows the worn surface and EDX results after the sliding test at 200 °C. Therein, Figure 10a shows low-magnification SEM micrographs, while Figure 11b shows high-magnification SEM micrographs of the worn surface. Apparently, the surface is almost covered by oxide debris (Figure 11a,b). The EDX measurements at points 3 and 4 (Figure 11c,d) verify the severely oxidized debris. However, it is assumed that abrasion played the main role, because the high carbon martensitic GCr15 steel remained hard at this temperature (about 746 HV [19]) and oxide debris were formed in greater amount and speed. Under this test condition, the oxidized debris could cause abrasion, just as in the case in three-body wear. This should be the reason for the highest wear rate and friction coefficient among the three conditions. Meanwhile, the wear of the counterpart became severe, too, leading to a higher wear rate compared to that at room temperature. Additionally, fatigue could contribute to the wear as in the case of the test at room temperature.

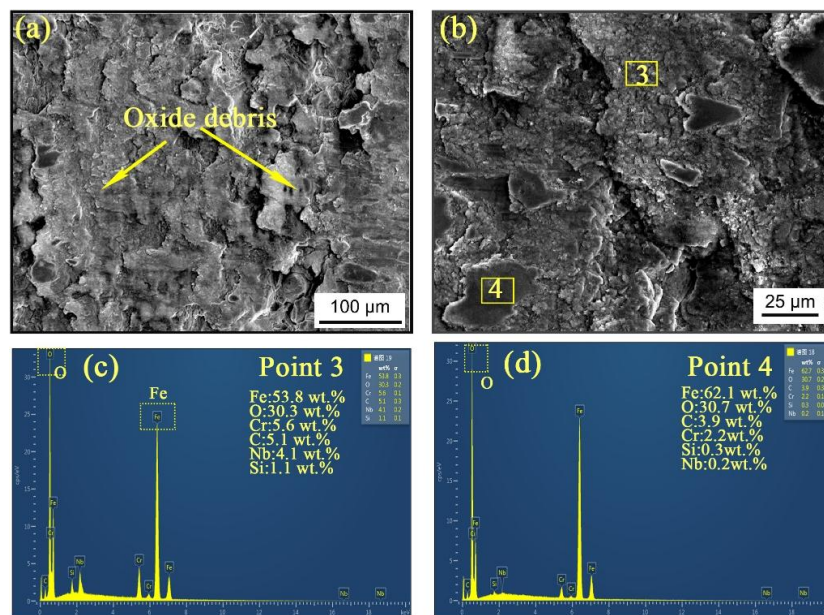


Figure 11. Typical worn surface morphologies and EDX results of $\text{Fe}_{59}\text{Cr}_{12}\text{Nb}_5\text{B}_{20}\text{Si}_4$ amorphous coating after sliding at 200 °C: (a) low-magnification; (b) high-magnification; (c) EDX result of point 3; and (d) EDX result of point 4.

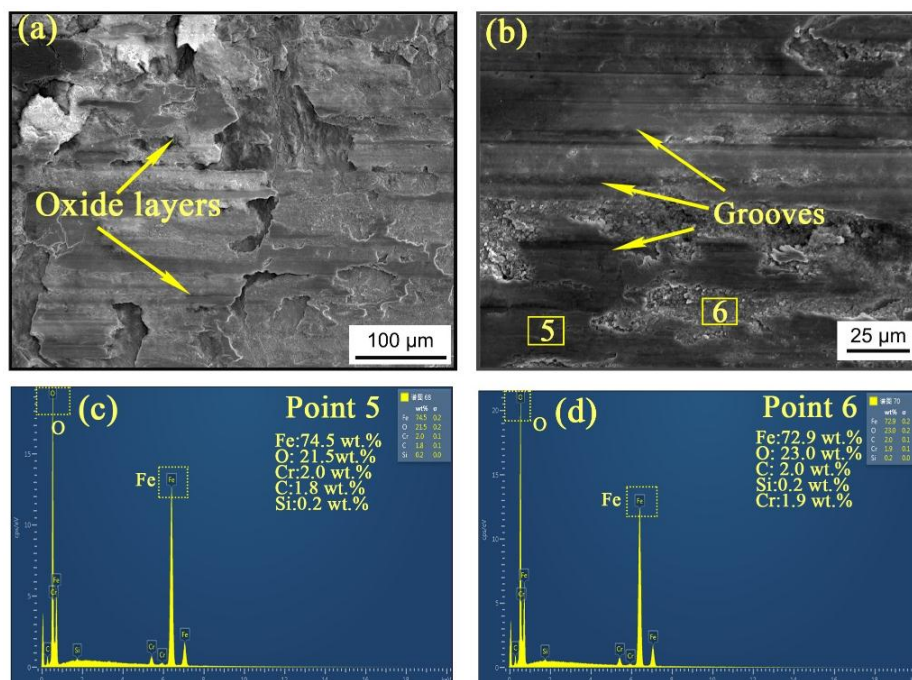


Figure 12. Typical worn surface morphologies and EDX results of $\text{Fe}_{59}\text{Cr}_{12}\text{Nb}_5\text{B}_{20}\text{Si}_4$ amorphous coating after sliding at 400 °C: (a) low-magnification; (b) high-magnification; (c) EDX result of point 5; and (d) EDX result of point 6.

Figure 12 reveals the low- and high-magnification SEM micrographs together with EDX results of the coating after sliding at 400 °C. Obviously, the surface is covered almost completely by oxide debris (Figure 12a). The EDX measurements at points 5 and 6 (Figure 12c,d) confirm wear debris were gravely oxidized. At the test temperature rises to 400 °C, the oxide debris was formed significantly faster owing to the aggravatingly tribological reaction. A covering compacted debris layer was formed

faster, correspondingly. At this temperature, the extensive oxide layers were much less abrasive and could work as solid lubricants [20,33,34], although some grooves are also observed (Figure 12b). In this way, the friction coefficient reached its stable stage much earlier than at room temperature and 200 °C, as shown in Figure 8. Correspondingly, the wear was also reduced, resulting in the lowest wear rate, as shown in Figure 9. In addition, due to the hardness of high carbon martensitic GCr15 steel decreased at this temperature (about 633 HV [19]), intensifies the wear of GCr15, leading to the highest wear rate compared to that at room temperature and 200 °C. Notably, as sliding at 400 °C, the actual contact temperature of friction surface during sliding process might be elevated and possibly higher than glass transition (T_g) and crystallization temperature (T_x) [35–37]. Hence, it is possible a subsequent crystallization took place. Nonetheless, it has been proved that the precipitated nanocrystal in amorphous could enhance its hardness and toughness, and increased its wear resistance [37–39]. Therefore, even if the contact temperature was higher than T_x , the formation of nanocrystals in amorphous matrix contributed to reduce the wear in this study.

4. Conclusions

The $\text{Fe}_{59}\text{Cr}_{12}\text{Nb}_5\text{B}_{20}\text{Si}_4$ amorphous coatings were prepared by HVOF spraying under two different conditions (denoted as H-1 and H-2). Both Fe-based coatings present dense, layered structures with porosities below 0.9% and extremely low oxygen contents on average of 0.16–0.18%. These reveal high process robustness during spraying of this alloy. Both amorphous coatings display much lower thermal conductivities than the reference stainless steel coating (5.85 W/(m·K)), indicating a good thermal barrier property. Therein, coating H-1 exhibits lower thermal conductivity (2.66 W/(m·K)) compared to coating H-2 (3.05 W/(m·K)) due to its higher amorphous phase content. Meanwhile the thermal diffusivity of H-1 coating displays limited increase with temperature up to 500 °C, which guarantees a steady thermal barrier ability on aluminum alloy. Furthermore, the amorphous coating shows better wear resistance compared to high carbon martensitic GCr15 steel from room temperature to 400 °C. As the temperature rises, the contribution of the tribological reaction is increased, leading to the friction coefficient and wear rate of coating are the highest at 200 °C and the lowest at 400 °C. Therefore, the $\text{Fe}_{59}\text{Cr}_{12}\text{Nb}_5\text{B}_{20}\text{Si}_4$ HVOF-sprayed coating developed in this study could be an available and proper candidate for MBTBCs application in vehicle engines where heat protection and associated wear resistance are simultaneously required.

Acknowledgments: The authors gratefully acknowledge the financial supports of the National Natural Science Foundation of China (51771005 and 51301009) and the Open Funds of the State Key Laboratory of Rare Earth Resource Utilization (RERU2017020 and RERU2016016).

Author Contributions: Zheng Zhou, Dingyong He, and Haihua Yao conceived and designed the experiments; Haihua Yao and Liang Wang performed the experiments and analyzed the data; Zhen Tan contributed materials/analysis tools; Haihua Yao wrote the paper; and Zheng Zhou and Lidong Zhao provided guidance and revised the paper.

Conflicts of Interest: The authors declare no conflict of interest.

References

1. Bobzin, K.; Ernst, F.; Zwick, J.; Schlaefler, T.; Cook, D.; Nassenstein, K.; Schwenk, A.; Schreiber, F.; Wenz, T.; Flores, G.; et al. Coating bores of light metal engine blocks with a nanocomposite material using the plasma transferred wire arc thermal spray process. *J. Therm. Spray Technol.* **2008**, *17*, 344–351. [[CrossRef](#)]
2. Poirier, D.; Lamarre, J.M.; Legoux, J.G. Thermal cycling assessment of steel-based thermal barrier coatings for Al protection. *J. Therm. Spray Technol.* **2015**, *24*, 175–184. [[CrossRef](#)]
3. Kim, J.K.; Xavier, F.A.; Kim, D.E. Tribological properties of twin wire arc spray coated aluminum cylinder liner. *Mater. Des.* **2015**, *84*, 231–237. [[CrossRef](#)]
4. Shin, D.; Gitzhofer, F.; Moreau, C. Properties and induction plasma sprayed iron based nanostructured alloy coatings for metal based thermal barrier coatings. *J. Therm. Spray Technol.* **2007**, *16*, 118–127. [[CrossRef](#)]

5. Dong, H.; Yang, G.-J.; Cai, H.-N.; Li, C.-X.; Li, C.-J. Propagation feature of cracks in plasma-sprayed YSZ coatings under gradient thermal cycling. *Ceram. Int.* **2015**, *41*, 3481–3489. [[CrossRef](#)]
6. Saucedo-Mora, L.; Slámečka, K.; Thandavamoorthy, U.; Marrow, T.J. Multi-scale modeling of damage development in a thermal barrier coating. *Surf. Coat. Technol.* **2015**, *276*, 399–407. [[CrossRef](#)]
7. Zhou, Z.; Wang, L.; He, D.Y.; Wang, F.C.; Liu, Y.B. Microstructure and electrochemical behavior of Fe-based amorphous metallic coatings fabricated by atmospheric plasma spraying. *J. Therm. Spray Technol.* **2011**, *20*, 344–350. [[CrossRef](#)]
8. Zhang, S.D.; Wu, J.; Qi, W.B.; Wang, J.Q. Effect of porosity defects on the long-term corrosion behaviour of Fe-based amorphous alloy coated mild steel. *Corros. Sci.* **2016**, *110*, 57–70. [[CrossRef](#)]
9. Zhou, Y.; Ma, G.; Wang, H.; Li, G.; Chen, S.; Wang, H.; Liu, M. Fabrication and characterization of supersonic plasma sprayed Fe-based amorphous metallic coatings. *Mater. Des.* **2016**, *110*, 332–339. [[CrossRef](#)]
10. Zheng, Z.B.; Zheng, Y.G.; Sun, W.H.; Wang, J.Q. Effect of heat treatment on the structure, cavitation erosion and erosion–corrosion behavior of Fe-based amorphous coatings. *Tribol. Int.* **2015**, *90*, 393–403. [[CrossRef](#)]
11. Koga, G.Y.; Schulz, R.; Savoie, S.; Nascimento, A.R.C.; Drolet, Y.; Bolfarini, C.; Kiminami, C.S.; Botta, W.J. Microstructure and wear behavior of Fe-based amorphous HVOF coatings produced from commercial precursors. *Surf. Coat. Technol.* **2017**, *309*, 938–944. [[CrossRef](#)]
12. Wang, Y.; Li, K.Y.; Scenini, F.; Jiao, J.; Qu, S.J.; Luo, Q.; Shen, J. The effect of residual stress on the electrochemical corrosion behavior of Fe-based amorphous coatings in chloride-containing solutions. *Surf. Coat. Technol.* **2016**, *302*, 27–38. [[CrossRef](#)]
13. Xu, P.; Zhang, C.; Wang, W.; Liu, L. Pitting mechanism in a stainless steel-reinforced Fe-based amorphous coating. *Electrochim. Acta* **2016**, *206*, 61–69. [[CrossRef](#)]
14. Shin, D.; Gitzhofer, F.; Moreau, C. Thermal property evolution of metal based thermal barrier coatings with heat treatments. *J. Mater. Sci.* **2007**, *42*, 5915–5923. [[CrossRef](#)]
15. Bobzin, K.; Oete, M.; Linke, T.F.; Koenigstein, T. Process development for innovative iron alloy metallic glass coating. *Adv. Eng. Mater.* **2016**, *18*, 1833–1840. [[CrossRef](#)]
16. Bobzin, K.; Oete, M.; Koenigstein, T. Investigation of amorphous/nanocrystalline iron-based thermal barrier coatings. *J. Therm. Spray Tech.* **2017**, *26*, 388–397. [[CrossRef](#)]
17. Barbezat, G. Advanced thermal spray technology and coating for lightweight engine blocks for the automotive industry. *Surf. Coat. Technol.* **2005**, *200*, 1990–1993. [[CrossRef](#)]
18. ASTM C633-01 Standard Test Method for Adhesion or Cohesion Strength of Thermal Spray Coatings; ASTM: West Conshohocken, PA, USA, 2008.
19. The Lucefin Group. Available online: http://www.lucefin.com/wp-content/files_mf/1.3505100cr6.pdf; http://www.lucefin.com/wp-content/files_mf/1.4404a31610.pdf (accessed on 15 August 2017).
20. Hou, G.; An, Y.; Zhao, X.; Zhou, H.; Chen, J. Effect of alumina dispersion on oxidation behavior as well as friction and wear behavior of HVOF-sprayed CoCrAlYTaCSi coating at elevated temperature up to 1000 °C. *Acta Mater.* **2015**, *95*, 164–175. [[CrossRef](#)]
21. Inoue, A. High strength bulk amorphous alloys with low critical cooling rates. *Mater. Trans. JIM* **1995**, *36*, 866–875. [[CrossRef](#)]
22. Takeuchi, A.; Inoue, A. Classification of bulk metallic glasses by atomic size difference, heat of mixing and period of constituent elements and its application to characterization of the main alloying element. *Mater. Trans.* **2005**, *46*, 2817–2829. [[CrossRef](#)]
23. Zhou, Z.; Wang, L.; Wang, F.; Zhang, H.; Liu, Y.B.; Xu, S. Formation and corrosion behavior of Fe-based amorphous metallic coatings by HVOF thermal spraying. *Surf. Coat. Technol.* **2009**, *204*, 563–570. [[CrossRef](#)]
24. Koutsky, J. High velocity oxy-fuel spraying. *J. Mater. Process. Technol.* **2004**, *157*, 557–560. [[CrossRef](#)]
25. Zhao, L.; Lugscheider, E. Influence of the spraying processes on the properties of 316L stainless steel coatings. *Surf. Coat. Technol.* **2002**, *162*, 6–10. [[CrossRef](#)]
26. Sun, B.; Fukanuma, H.; Ohno, N. Study on stainless steel 316L coatings sprayed by a novel high pressure HVOF. *Surf. Coat. Technol.* **2014**, *239*, 58–64. [[CrossRef](#)]
27. Kingery, W.D.; Bowen, H.K.; Uhlmann, D.R. *Introduction to Ceramics*, 2nd ed.; John Wiley & Sons: Hoboken, NJ, USA, 1976.
28. Sietsma, J.; Thijssse, B.J. Characterization of free volume in atomic models of metallic glasses. *Phys. Rev. B Condens. Mater.* **1995**, *52*, 3248–3255. [[CrossRef](#)]

29. Lu, Y.; Huang, Y.; Wei, X.; Shen, J. Close correlation between transport properties and glass-forming ability of a FeCoCrMoCBy alloy system. *Intermetallics* **2012**, *30*, 144–147. [[CrossRef](#)]
30. Chi, W.G. Thermal Transport Properties of Thermally Sprayed Coatings: An Integrated Study of Materials, Processing and Microstructural Effects. Ph.D. Thesis, Stony Brook University, Brook, NY, USA, December 2007.
31. Yamasaki, M.; Kagao, S.; Kawamura, Y. Thermal diffusivity and conductivity of Zr₅₅Al₁₀Ni₅Cu₃₀ bulk metallic glass. *Scr. Mater.* **2005**, *53*, 63–67. [[CrossRef](#)]
32. Umetsu, R.Y.; Tu, R.; Goto, T. Thermal and electrical transport properties of Zr-based bulk metallic glassy alloys with high glass-forming ability. *Mater. Trans.* **2012**, *53*, 1721–1725. [[CrossRef](#)]
33. Wood, P.D.; Evans, H.E.; Ponton, C.B. Investigation into the wear behaviour of stellite 6 during rotation as an unlubricated bearing at 600 °C. *Tribol. Int.* **2011**, *44*, 1589–1597. [[CrossRef](#)]
34. Inman, I.A.; Datta, P.K.; Du, H.L.; Burnell-Gray, J.S.; Luo, Q. Microscopy of glazed layers formed during high temperature sliding wear at 750 °C. *Wear* **2003**, *254*, 461–467. [[CrossRef](#)]
35. Fleury, E.; Lee, S.M.; Ahn, H.S.; Kim, W.T.; Kim, D.H. Tribological properties of bulk metallic glasses. *Mater. Sci. Eng. A* **2004**, *375–377*, 276–279. [[CrossRef](#)]
36. Kong, J.; Xiong, D.; Li, J.; Yuan, Q.; Tyagi, R. Effect of flash temperature on tribological properties of bulk metallic glasses. *Tribol. Lett.* **2009**, *35*, 151–158. [[CrossRef](#)]
37. Rahaman, M.L.; Zhang, L.C.; Ruan, H.H. Understanding the friction and wear mechanisms of bulk metallic glass under contact sliding. *Wear* **2013**, *304*, 43–48. [[CrossRef](#)]
38. Inoue, A.; Wang, X. Bulk amorphous FC₂₀(Fe–C–Si) alloys with small amounts of B and their crystallized structure and mechanical properties. *Acta Mater.* **2000**, *48*, 1383–1395. [[CrossRef](#)]
39. Cheng, J.; Liang, X.; Wang, Z.; Xu, B. Dry sliding friction and wear properties of metallic glass coating and martensite stainless coating. *Tribol. Int.* **2013**, *60*, 140–146. [[CrossRef](#)]



© 2017 by the authors. Licensee MDPI, Basel, Switzerland. This article is an open access article distributed under the terms and conditions of the Creative Commons Attribution (CC BY) license (<http://creativecommons.org/licenses/by/4.0/>).